Computers in Biology and Medicine 111 (2019) 103349

Contents lists available at ScienceDirect

Computers in Biology and Medicine

journal homepage: www.elsevier.com/locate/compbiomed

Visualization of interpolated atrial fiber orientation using evenly-spaced streamlines

Ariane Saliani[a,b], Alena Tsikhanovich[a,b], Vincent Jacquemet[a,b,*]

[a] Université de Montréal, Département de Pharmacologie et Physiologie, Institut de Génie Biomédical, Montréal, Canada
[b] Hôpital du Sacré-Coeur de Montréal, Centre de Recherche, Montréal, Canada

ARTICLE INFO

Keywords:
Orientation field interpolation
Streamline integration
Anisotropy
Atrial fiber structure
Cardiac modeling

ABSTRACT

Background: Mathematical models of electrical propagation in the atria necessitate the specification of fiber orientation, often visualized over the epicardial and endocardial surfaces. Clear graphical representation of an orientation field over a surface remain challenging, which hinders the comparison between published models.
Method: A method for the placement of evenly-spaced streamlines over a triangulated surface is proposed. Streamlines tangent to an orientation field are integrated, starting from a set of seed points. Distribution of seed points can be either uniformly random or located in the vicinity of existing streamlines. Stopping conditions are designed to prevent streamlines from getting closer than a threshold referred to as the separation distance. At each iteration, the longest among candidate streamlines is kept. Streamlines are finally rendered on the surface as tubes. The outcome is assessed subjectively by visual inspection and objectively by measuring average streamline length and average lateral distance between streamlines.
Results: Fiber orientation fields are conveniently created by angle-based interpolation from fiber tracts manually drawn based on literature review. The zebra-like representation of evenly-spaced streamlines enables clear identification of local fiber orientation. The results show that streamline density can be controlled since the lateral distance between streamlines is guaranteed to vary between 1 and 2 times the separation distance. Average streamline length can be increased by using more seed points, which offers a trade-off between quality and speed.
Conclusion: Evenly-spaced streamline visualization of fiber orientation facilitates the description and the comparison of fiber structure in computer models of the atria.

1. Introduction

Computer models of electrical propagation in the atria have been developed to investigate the triggers, the perpetuation mechanisms, the complex dynamics, the diagnosis and the treatments of atrial arrhythmias [1]. Since the conduction properties of the cardiac muscle are anisotropic, these models require knowledge about fiber structure. Specification of local fiber orientation is typically based on anatomical description of major fiber tracts and gross fiber structure or constructed from image-derived atlases [2–6]. This information can be mapped onto a geometrical model of the atria using landmark points [7,8], anatomically-driven coordinate systems [9] or non-rigid registration [10]. Then, combined with the specification of longitudinal and transverse conductivity including possible local alterations caused by fibrosis [11], electrical propagation can be simulated [1].

Comparison of fiber orientation between published models from the articles alone remains difficult. A potential issue is inter-individual variability in anatomy and fiber structure [5]. Another one is visualization. Among different available graphical representations, the interpretation of color-coded fiber angles [2] requires significant mental effort, quiver plots on unstructured meshes are often constrained to have irregularly-spaced and too small arrows [9,12–14], line integral convolution representations [8] look nice but noisy and are only locally coherent, and 3D tractography [5,15,16] works at its best when displaying an individual bundle of fibers. Despite their qualities, these methods hardly match the clarity of old-style manual drawings of gross fiber structure by anatomists [17].

Similar conclusions have been reached in the field of fluid velocity flow visualization [18]. This led to the development of computer graphics techniques for evenly-spaced placement of streamlines in 2D geometries [19,20]. Several improvements [21,22], extension to 3D [23] and projection on a 3D surface [24,25] have been proposed. These

* Corresponding author. Hôpital du Sacré-Coeur de Montréal, Centre de Recherche, 5400 boul. Gouin Ouest, Montreal, Quebec, H4J 1C5, Canada.
E-mail address: vincent.jacquemet@umontreal.ca (V. Jacquemet).

https://doi.org/10.1016/j.compbiomed.2019.103349
Received 13 April 2019; Received in revised form 4 June 2019; Accepted 2 July 2019

approaches seem to be well adapted for the visualization of fiber orientation fields. Note that orientation fields differ from velocity flow fields in that they are static, have no magnitude and no direction of propagation, which has an impact on streamline integration and stopping criteria.

Several recent models of atrial fiber orientation are constructed from three surfaces [7,9]: the left atrial epicardial surface, the left endocardial surface and the right epicardial surface. The right atrial trabeculated structure and the inter-atrial connections are handled separately, like in previous models [26]. Then, either two layers are simulated [9] or fiber orientation is interpolated within the thickness [8]. In the continuity of these works, the aim of our paper is to develop and validate an algorithm for evenly-spaced streamline placement on a triangulated surface with an orientation field. Our method is inspired by the 2D algorithm of Jobard et al. [20] and differs from it by the choice of data structures more suited to our specific problem on a 3D surface. Instead of focusing on the non-hidden faces of the mesh like the image-based approach by Spencer et al. [24], streamlines will be generated over the whole surface. Test cases will be generated by a new method for fiber orientation interpolation from major fiber tracts on a surface.

2. Methods

The structure of this section is illustrated by the algorithm workflow shown in Fig. 1.

2.1. Parameterization of fiber orientation

Due to the thinness of the atria, fiber orientation is generally visualized on a surface. Mathematically, this surface is a manifold S that has one or more boundaries. In this work, it will be assumed that fiber orientation on that surface is defined by fiber tracts described by a set of curves lying on the surface. These fiber tracts may be drawn manually on the surface based on published anatomical data or mapped onto it using an atlas or a rule-based approach.

Fiber orientation may be represented by a vector field $\mathbf{v}(\mathbf{x})$, $\mathbf{x} \in S$, tangent to the fiber tracts. Note that the orientation vector is defined up to a negative sign, i.e. $\mathbf{v}(\mathbf{x})$ and $s(\mathbf{x})\,\mathbf{v}(\mathbf{x})$ define the same orientation for any (possibly discontinuous) function s such that $s(\mathbf{x}) = \pm 1$. The vector field $\mathbf{v}(\mathbf{x})$ may not be continuous. In fact, it may be impossible to create a smooth vector field that represents an orientation field, as shown by the counter-example of an orientation rotating by half a turn along a closed curve, similarly to a Moebius stripe. This is another difference between flow velocity fields and orientation fields.

These remarks suggest to define local orientation using an angle θ in the range $(-\pi/2, \pi/2]$. If there is a local orthonormal basis $(\mathbf{e}_l(\mathbf{x}), \mathbf{e}_t(\mathbf{x}))$ for $\mathbf{x} \in S$, varying smoothly as a function of $\mathbf{x}$ and without singularity, then the local transforms between angle and vector can be defined as:

$$\theta = \text{sign}(\mathbf{v}\cdot\mathbf{e}_l)\,\arcsin\frac{\mathbf{v}\cdot\mathbf{e}_t}{||\mathbf{v}||} \tag{1}$$

$$\mathbf{v} = \cos(\theta)\cdot\mathbf{e}_l + \sin(\theta)\cdot\mathbf{e}_t\,. \tag{2}$$

Clearly, $\theta \in (-\pi/2, \pi/2]$ and $\theta(-\mathbf{v}) = \theta(\mathbf{v})$, with the (unusual) convention that $\text{sign}(0) = 1$. A vector parallel to $\mathbf{e}_l$ (longitudinal) is mapped to $\theta = 0$ and a vector parallel to $\mathbf{e}_t$ (transverse) is mapped to $\theta = \pi/2$. Reduction in dimension from 3 (vector $\mathbf{v}$) to 1 (scalar θ) will facilitate interpolation. However, it requires $\theta(\mathbf{x})$, and consequently $\mathbf{e}_l(\mathbf{x})$ and $\mathbf{e}_t(\mathbf{x})$ to be all smooth functions of $\mathbf{x}$.

2.2. Reference orientation field

The reference orientation field needed for the interpolation procedure will be any smooth vector field $\mathbf{v}_0(\mathbf{x})$ such that $\mathbf{v}_0(\mathbf{x}) \neq 0$, $\forall\ \mathbf{x} \in S$. It is important to note that this field does not need to have any physiological relevance; it will only be used for interpolation. The local basis will be reconstructed as $\mathbf{e}_l = \mathbf{v}_0/||\mathbf{v}_0||$ and $\mathbf{e}_t = \mathbf{n} \times \mathbf{e}_l$, where $\mathbf{n}(\mathbf{x})$ is the outward-oriented normal to the surface.

The smoothness condition prevents the use of coordinate systems with a singularity such as the north pole of spherical coordinates or near the left atrial appendage in the universal atrial coordinate system [9]. Singular coordinate systems can be used for specifying the location of fiber tracts, but another system needs to be constructed for orientation field interpolation.

A simple approach is to derive $\mathbf{v}_0$ from the gradient of a coordinate variable u, i.e. $\mathbf{v}_0 = \nabla u$, where $\nabla^2 u = 0$ with $u = 1$ on a boundary (e.g. a valve) and $u = 0$ on another boundary (e.g. the fossa ovalis or septum) [9]. By the maximum principle, u cannot have a global maximum within the interior of the domain, but u might have a critical point, which would create a singularity $\mathbf{v}_0 = 0$. To eliminate any risk of singularity, a solution is to map the surface onto a planar domain using a surface parameterization technique. For triangulated surfaces, one of the options is the Floater et al. mean value parameterization that maps a surface with a border (e.g. a valve) onto a disk [27]. The resulting map $p_D(\mathbf{x})$ is guaranteed to be bijective when the border of the surface is convex. The computational geometry package CGAL provides an implementation of that method [28].

After the surface is mapped onto the disk, the Laplace equation $\nabla^2 u_D = 0$ for the coordinate variable u_D defined on the disk D is solved with $u_D = 1$ on the outer border (circle) and $u_D = 0$ on an inner boundary such as the fossa ovalis. To reduce distortions around other boundaries, notably the pulmonary veins, these boundaries are ignored

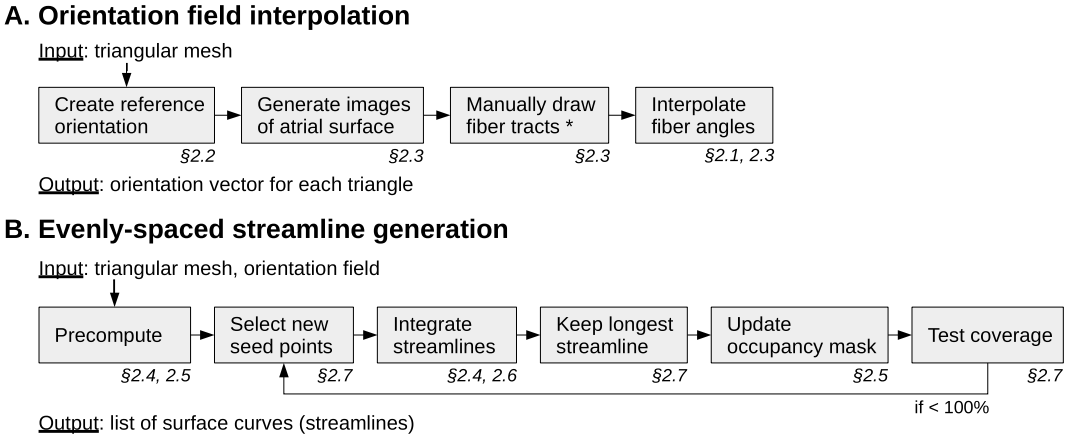

Fig. 1. Overview of the algorithm workflow: (A) orientation field interpolation on a triangulated surface; (B) generation of evenly-spaced streamlines on a surface. References to the relevant subsections are indicated below the boxes. The asterisk highlights human intervention.

(i.e. the holes are filled). Under these assumptions, it can be shown that ∇u_D cannot vanish [29]. The solution u_D is then mapped back onto the surface using $u(\mathbf{x}) = p_D^{-1}(u_D(\mathbf{x}))$, and the reference coordinate system $(\mathbf{e}_l(\mathbf{x}), \mathbf{e}_t(\mathbf{x}))$ is derived from the gradient of u. This procedure only has to be performed once to generate a reference vector field $\mathbf{v}_0$ for the surface S.

2.3. Orientation field specification and interpolation

Among different ways to input surface curves, we chose an image-based approach. The 3D triangulated surface is displayed on the screen and saved as an image. The transform from 3D coordinates to image pixels is stored (based on the model-view matrix in OpenGL [30]). Curves are drawn manually on the image using the pencil tool of a paint program (GIMP/GNU Image Manipulation Program) to provide maximum flexibility. Then, bitmap curves are segmented (connected components) and vectorized ('autotrace' package in Linux distributions). The triangulated surface is projected on the image using the 3D-to-pixels transform. Intersection between a vectorized curve and the projected triangular mesh gives a sequence of points on mesh edges that defines a curve on the 3D surface.

On each triangle intersecting a surface curve, the orientation vector is set to the tangent vector and the angle θ is computed from (1). As in phase map interpolation [31,32], a complex phase transform is applied to avoid phase wrapping issues. Because θ only covers a range of length π, the complex phase φ is defined as $\varphi = \exp(2i\theta)$. When fiber orientation is assumed to be following the border of a boundary, the complex phase is specified accordingly on the boundary vertices. Otherwise, von Neumann boundary condition is assumed. The complex phase is then interpolated using Laplacian interpolation, and the vector field $\mathbf{v}$ is reconstructed from (2) with $\theta = \frac{1}{2}\arg\varphi$. There may be points where φ is zero. Around these singularities, fiber orientation changes abruptly. These situations may be topologically unavoidable.

2.4. Integration of streamlines

Unlike in fluid dynamics, our streamlines are not oriented since the sign of the vector is irrelevant. In a triangular mesh where the vector field is assumed to be constant in each triangle, streamlines are polygonal lines with vertices lying on edges. Streamlines are therefore encoded as a sequence of edge identifiers and relative positions along the edge (coordinate $s \in [0,1]$, $s = 0$ and $s = 1$ corresponding to the endpoints of the edge). They start at a so-called seed point on an edge and propagate in both directions, jumping from edge to edge [33]. These successive points are called the sample points of the streamline. This process is illustrated in Fig. 2.

In a triangle $P_0P_1P_2$, the edge vectors P_0P_1 and P_0P_2 are denoted respectively by $\mathbf{x}_1$ and $\mathbf{x}_2$. Without restriction to the generality, the seed point is assumed to be located on the P_1P_2 edge at $P_0 + (1-s)\,\mathbf{x}_1 + s\,\mathbf{x}_2$. The orientation vector is expressed in the local basis as $\mathbf{v} = \alpha_1\mathbf{x}_1 + \alpha_2\mathbf{x}_2$. The critical coordinate s_c is defined as $s_c = \alpha_2/(\alpha_1 + \alpha_2)$. Note that $s_c(-\mathbf{v}) = s_c(\mathbf{v})$. Algebraic calculations show that the next point of the streamline is determined entirely by s and s_c. If $0 < s/s_c < 1$, the next point is $P_0 + (1 - s/s_c)\,\mathbf{x}_1$. Otherwise, the next point is $P_0 + (s - s_c)/(1 - s_c)\cdot\mathbf{x}_2$. This rule is applied iteratively to reconstruct a streamline until one of the stopping criteria described in subsection 2.6 is satisfied. Since s_c depends only on the geometry and vector field, it can be precomputed for the three edges of each triangles. Degenerate cases $s_c = 0$, 1 or ∞ and $s = 0$ or 1 can be handled by infinitesimal change in orientation vector or streamline sample point position unless very high accuracy is needed.

2.5. Occupancy mask

In order to prevent streamlines from becoming closer than a separation distance d_{sep} from each other, it is necessary to create a data structure that keeps track of previously inserted streamlines [20]. Grid data structures may be used to search in the list of all streamline points, as done with vector fields on 2D and 3D regular grids [20,23]. Because streamline sample points are restricted to be on edges of the triangular mesh (see previous subsection), we opted for an occupancy mask instead. This data structure stores for each edge of the mesh a 64-bit mask describing whether each of 64 sub-segments of the edge are at a distance smaller than d_{sep} from another streamline (Fig. 2). Testing if a point on an edge is too close to a streamline is therefore straightforward.

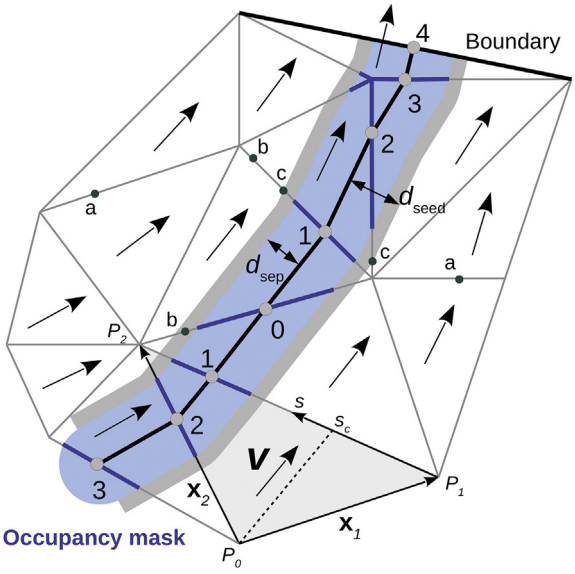

Fig. 2. Streamline integration and occupancy mask. The orientation vector $\mathbf{v}$ in each triangle of the surface S is displayed as an arrow. The sample points of the streamline (light gray circles) are numbered from 0 to 4 and run in both direction starting from the seed point (number 0) until it hits a boundary or is stopped by another criterion. The light blue area represents the set of points at a distance smaller than d_{sep} from the streamline. The dark blue edge segments indicate where the occupancy mask is set to 1. The dark gray dots marked by an 'a' denote possible seed point candidates for the 'random' streamline placement method. The dots 'b' are seed point candidates for the 'neighborhood' method. The dots 'c' are at a distance d_{seed} from the baseline as delimited by the light gray area extending the occupied region, and correspond to the 'distance' method.

This approach involves two approximations. First, d_{sep} must be larger than edge length divided by 64. The resolution of our mesh is 1 mm which gives 15 μm accuracy for the occupancy mask. The bit-length of the bitmask could be extended if needed. Second, the masked region is assumed to have a polygonal shape since the occupancy mask only stores the intersection between the masked region and the edges (Fig. 2). This is only an approximation (see below). Nevertheless, the occupancy mask remains accurate on the edges, where the sample points of the streamline lay. This means that our streamlines might be longer than what they should, but not shorter.

Updating the occupancy mask is more involved. The set of points located at a Euclidean distance smaller than d_{sep} from a streamline is the union of spheres centered on the sample points of the streamline and cylinders aligned with streamline segments, all of them with a radius of d_{sep}. The intersections between the spheres/cylinders and the edges of the mesh are computed, the bits corresponding to edge sub-segments located inside the spheres/cylinders are set to 1 and these sub-segments are said to be occupied (Fig. 2). To accelerate computations, the list of edges located at a distance smaller than d_{sep} from each triangle is precomputed. An advantage of these precomputations is that since the edges are looped over using breadth-first search, edges that are close to the triangle in terms of Euclidean distance but belong to another branch

of the surface can be excluded, i.e. the list of neighboring edges is guaranteed to be connected. This mitigates possible discrepancies between Euclidean and geodesic distance. This issue would be more difficult to deal with if kd-tree search was used. On the other hand, a disadvantage of the occupancy mask approach is that one cannot remove a streamline from it.

2.6. Stopping criteria

Streamline integration is stopped when one of the five following conditions occurs: (1) the maximum number of iterations (typically 1024, which sets buffer size) is reached; (2) the streamline hits a boundary; (3) the streamline becomes too close to another streamline as indicated by the occupancy mask; (4) the streamline undergoes an abrupt change in direction or a U-turn; (5) a segment of the streamline becomes too close to another part of that same streamline.

Criteria 1 to 3 have been described in previous subsections. The maximum number of iterations can be set to an upper bound of plausible streamline length (e.g. 1 m) divided by the spatial resolution Δx. Criterion 4 occurs when the angle between the orientation vectors of two adjacent triangles is larger than a threshold value ($\pi/2$ by default; a threshold of π disables the criterion). Interestingly, this condition does not depend on where on the common edge the streamline arrives and in which direction it propagates. This means that criterion 4 can be precomputed for all edges.

Criterion 5 refers to nearly periodic streamlines [20]. This occasionally occurs when fibers are winding around a vein. It is conveniently implemented as clean-up step after streamline integration. The streamline is then shortened in order to satisfy the requirement. First, a kd-tree of the streamline sample points is constructed and the list of pairs of points with distance smaller than d_{sep} is extracted (cKDTree.query_pairs from scipy.spatial in python). Some of the pairs may be consecutive sample points along the streamline. To tackle this problem, the curvilinear coordinate (from 0 to L where L is the length of the streamline) is computed and only the pairs such that the difference in curvilinear coordinate is larger than $2\,d_{sep}$ are kept. Scanning the streamline from an extremity, the streamline is cut when the second point of any pair is reached. The remaining of the streamline is discarded.

2.7. Streamline placement

Streamline placement consists in selecting seed point candidates for streamline integration. The target is to achieve maximal coverage, larger streamline length and higher streamline density. Coverage is defined as the percentage of the surface covered by streamlines and is estimated from the occupancy mask. Streamline placement stops when coverage is 100% which means that no more streamline can be inserted. Average streamline length L_{avg} is reported. Streamline density is assessed using an approximation of the average spacing between streamline computed as $d_{avg} = A/(n\,L_{avg})$ where n is the number of streamlines and A is the total area of the surface. In principle, $d_{avg} > d_{sep}$. We will test the hypothesis that the ratio d_{avg}/d_{sep} is independent from d_{sep}.

Different strategies have been proposed for streamline placement in regular grids [19,20,23]. The most successful approach has been to select seed points in the vicinity of already placed streamlines [18]. Adapting these previous works to triangulated surfaces, streamlines are placed one by one in successive steps. At each step, n_{seeds} seed point candidates are randomly drawn from a list of admissible locations.

These admissible locations, some of which are shown in Fig. 2, are chosen using one of the three following approaches: (1) In the 'random' method, all points outside the occupancy mask are admissible. (2) In the 'neighborhood' method, admissible points are in the unoccupied part of partially occupied edges. This guarantees that seed points are within a distance ranging from d_{sep} to $d_{sep} + \Delta x$ from an existing streamline, where Δx is the edge length. (3) In the 'distance' method, admissible points are at a distance of $d_{seed} = c_{seed} \cdot d_{sep}$ (where c_{seed} is equal to 1.3 [20]) of already placed streamlines. These points are identified by intersecting cylinders constructed along the streamline with the surface in a way similar to occupancy mask update. Points located in occupied sub-segments are discarded. If no admissible point can be found (for example in the first step), seed points are randomly drawn within completely unoccupied edges.

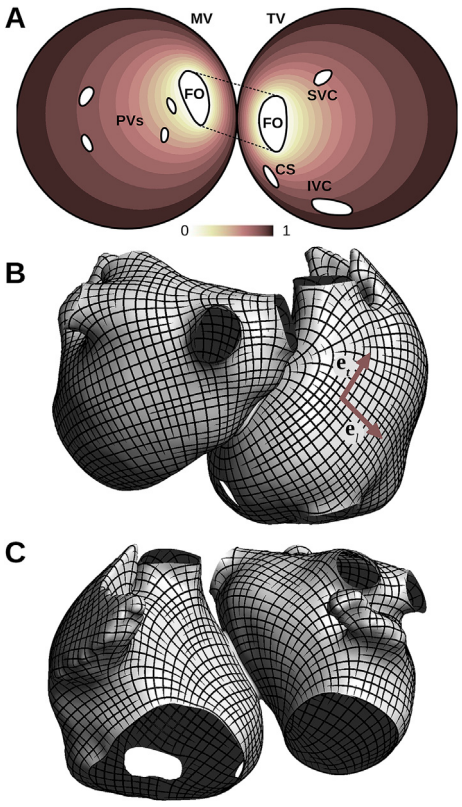

Fig. 3. Generation of the reference orientation for interpolation. (A) Planar surface parameterization. The field u_D is color-coded. The boundaries are shown: pulmonary veins (PVs), fossa ovalis (FO), superior and inferior vena cavae (SVC and IVC), coronary sinus (CS) and the mitral and tricuspid valves (MV and TV, the exterior borders). The relative sizes of the holes are not physiological because the mapping $p_D(\mathbf{x})$ does not preserve area. (B) Posterior view of the atrial geometry. Streamlines along and orthogonal to the orientation field $\mathbf{v}_0(\mathbf{x})$ are displayed. An example of local basis vectors ($\mathbf{e}_l$, $\mathbf{e}_t$) is shown. (C) Anterior view.

Streamlines are constructed for each seed point candidate without updating the occupancy mask. Following a greedy algorithm design, only the longest candidate streamline is kept and the occupancy mask is updated accordingly. This is expected to increase L_{avg}. When the occupancy mask is fully covered, the iterations stop. By construction, at the end of the procedure, the distance between a streamline and its nearest neighbor is at least d_{sep} and at most $2\,d_{sep}$. Otherwise, another streamline would have been inserted between the two.

2.8. Streamline rendering

Streamlines are displayed as tubes. For this purpose, a regular polygon (4–8 sides) is extruded along the streamline. The normal to the (atrial) surface helps keeping the alignment between the vertices of successive polygons. The resulting tube is triangulated. Tapering consists in making the extremities of each streamline look thinner. Tapering is often performed by image post-processing [19], but is here implemented as a variation of the tube radius ρ along the streamline:

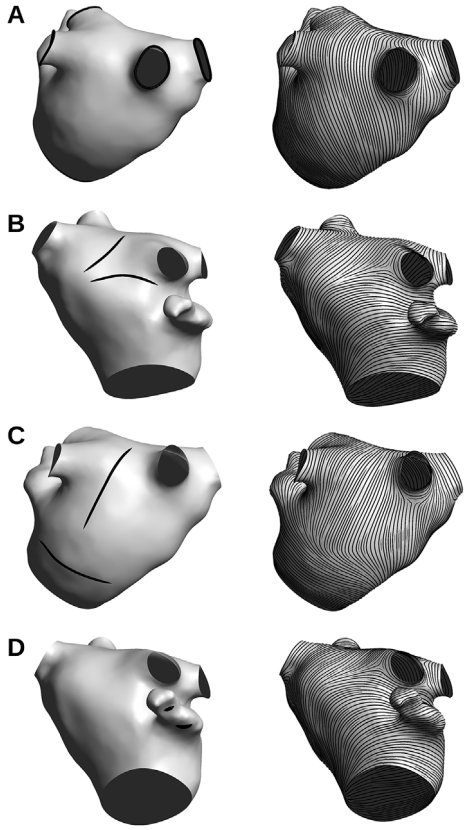

Fig. 4. Step-wise specification of gross fiber orientation by successive addition of fiber tracts. The manually-drawn fiber tracts are shown on the left panels and the resulting fiber orientation on the right panels. (A) Boundary conditions only; (B) anterior view; (C) posterior view; (D) small fiber tracts in the appendage. Visualization parameters: $d_{sep} = 0.8$ mm and $n_{seeds} = 1000$ with the 'neighborhood' placement method.

$$\rho(s) = \rho_0 \left(1 - e^{-s/\lambda}\right)\left(1 - e^{-(L-s)/\lambda}\right), \tag{3}$$

where s is the curvilinear coordinate along the streamline, L is the streamline length, ρ_0 is the nominal tube radius and λ is the tapering length scale. We used $\rho_0 = 0.18$ mm and $\lambda = 2$ mm.

2.9. Implementation and validation

The code has been mostly written in python with some critical parts such as streamline integration and occupancy mask operations written in C++ interfaced using cython. The visualization code, built upon pyopengl, is separated from the streamline placement software. There has been no attempt to achieve real-time streamline computation. With some minimal optimizations, the execution times range from 0.5 s to a few seconds (unless $n_{seeds} \gg 100$ or if $d_{sep} \ll 1$ mm). The final geometry with the streamlines, though, can be rotated in real time.

The test case is a model of the left and right atria [34]. Its triangular mesh represents the midmyocardium surface and is composed of 43,679 triangles with a resolution of about 1 mm. The part of the septum wall that is common to both atria, referred to as the fossa ovalis in the methods, is not included since it is intended to be handled separately, like the inter-atrial connection bundles. The fossa ovalis therefore creates a hole in both atrial surfaces in this model.

3. Results

3.1. Local basis vectors

The procedure for determining the local basis vectors ($\mathbf{e}_l(\mathbf{x})$, $\mathbf{e}_t(\mathbf{x})$) is illustrated in Fig. 3. Panel A shows how the atrial geometry is unfolded to define a planar parameterization of the surface. The gradient of the field $u(\mathbf{x})$, color-coded in panel A, is represented as streamlines on panel B and C. Its orthogonal field, computed as the cross product with the vector normal to the surface, is also displayed. This illustrates the local basis vectors (right side of panel B). The streamlines appear to be separated by a distance ranging from d_{sep} to $2\,d_{sep}$. This is particularly clear where streamlines are slowly converging or diverging.

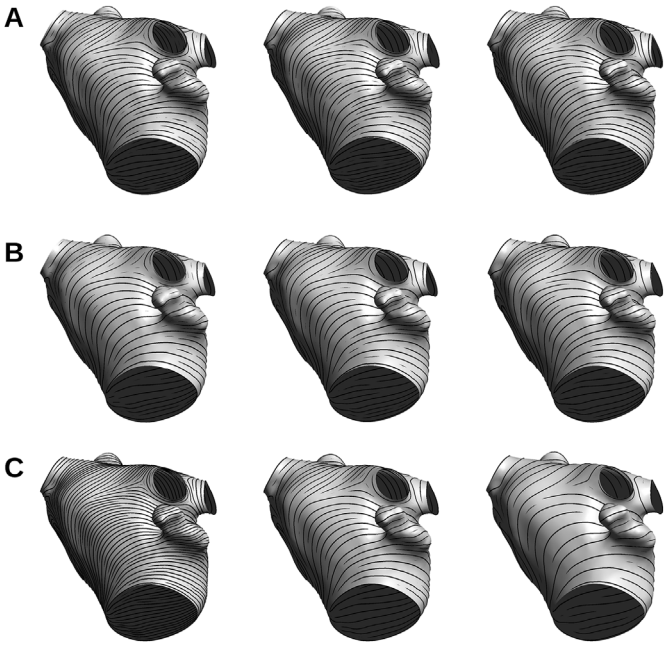

Fig. 5. Examples of visualization of the fiber orientation of Fig. 4D using different sets of parameters. (A) Placement methods 'random', 'neighborhood' and 'distance' respectively from left to right, with $n_{seeds} = 1$ and $d_{sep} = 1.5$ mm; (B) 'neighborhood' placement with $d_{sep} = 2$ mm and $n_{seeds} = 1$, 10 and 1000 from left to right; (C) 'random' placement with $n_{seeds} = 1000$ and $d_{sep} = 1$, 2 and 3 mm from left to right.

3.2. Orientation field interpolation

A simple step-by-step example of fiber orientation interpolation in the left atrium is shown in Fig. 4. Boundary conditions (fibers parallel to the boundaries) are sufficient to generate a reasonable, but not physiologically-accurate orientation field (panel A). The addition of fiber tracts corresponding to (part of) the Bachmann's and septopulmonary bundles improves the anterior left atrial wall (panel B). T-shaped lines enable the design of abrupt transition of fiber orientation (panel C). Short lines in the appendage illustrate the ability to fine tune local orientation (panel D). Gross fiber orientation can therefore be specified using a limited number of lines.

3.3. Visualization parameters

Fig. 5 shows how visualization parameters affect the output image. The placement method (panel A) does not appear to have a major impact although the 'distance' method (last on the right) seems to have slightly longer streamlines. A larger number of seed points improves the maximization of streamline length, which can be seen in panel B. The minimal separation distance d_{sep} controls the distance between streamlines (panel C).

These observations are quantified and summarized in Fig. 6 using the average streamline length (L_{avg}) and the (approximate) lateral distance between streamline (d_{avg}). Average length L_{avg} is larger when more seed points are considered and when the separation distance d_{sep}

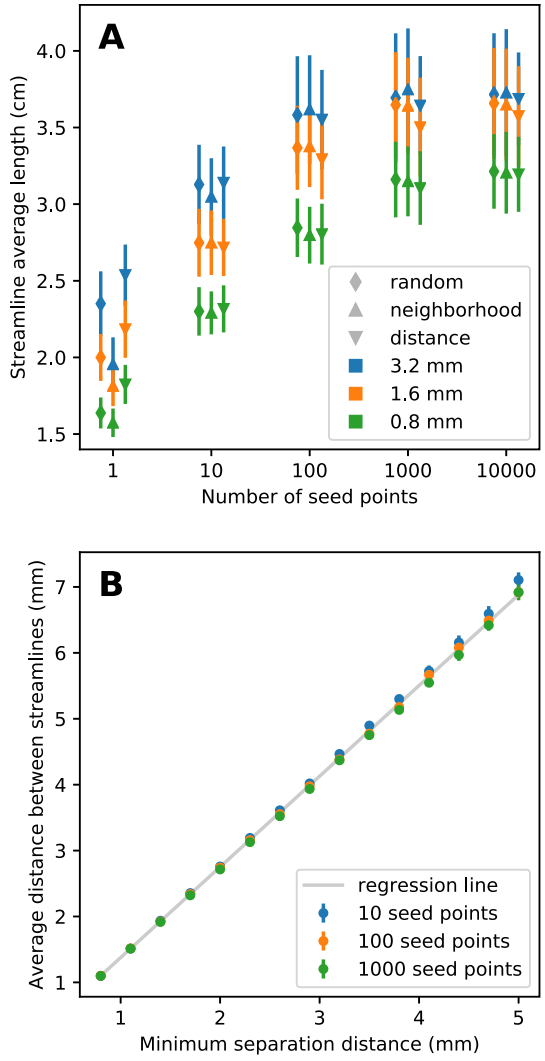

Fig. 6. (A) Average length of streamlines (L_{avg}) for 5 logarithmically-spaced values of the number of seed points (n_{seeds}). The minimum separation distance (d_{sep} = 0.8, 1.6 and 3.2 mm) is color-coded. Marker shape denotes the streamline placement method. Error bars are standard deviations over 16 realizations of the streamline representation of the four fiber orientation fields of Fig. 4 (B) Average distance between streamlines (d_{avg}) as a function of d_{sep} for the three placement methods. The number of seed points (n_{seeds}) is color-coded. Error bars show standard deviation as in panel A. The regression line is d_{avg} = 1.376 d_{sep} based on 540 data points.

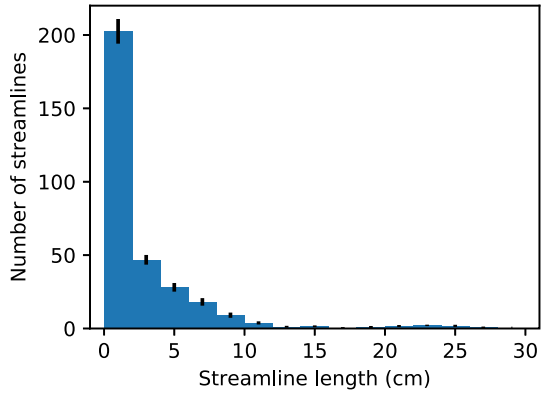

Fig. 7. Histogram of streamline lengths for the orientation field of Fig. 4D using the 'neighborhood' placement method with d_{sep} = 0.08 mm and n_{seeds} = 1000. Error bars are standard deviations over 16 realizations of streamline generation.

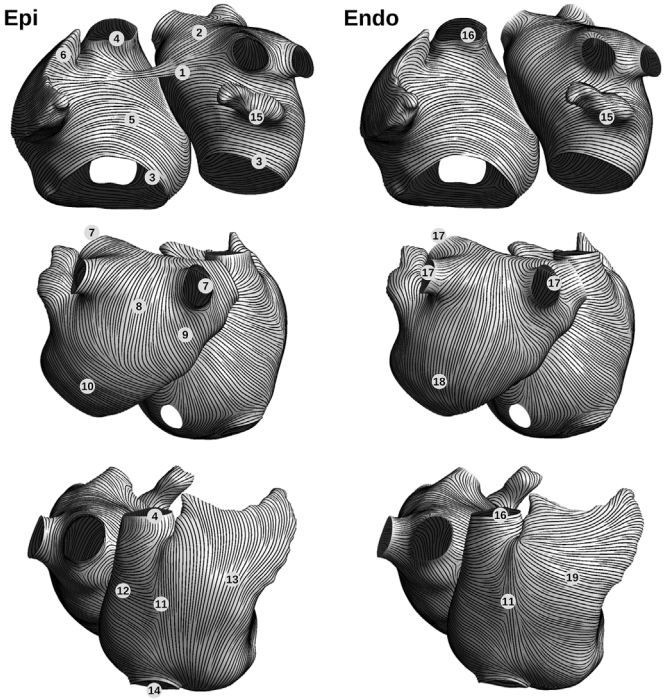

Fig. 8. Example of fiber orientation field in the epicardial (left panels) and endocardial surfaces (right panels). Three views of the same fiber structure are provided (top, middle and bottom rows). The circled numbers refer to the rows of Tables 1 and 2

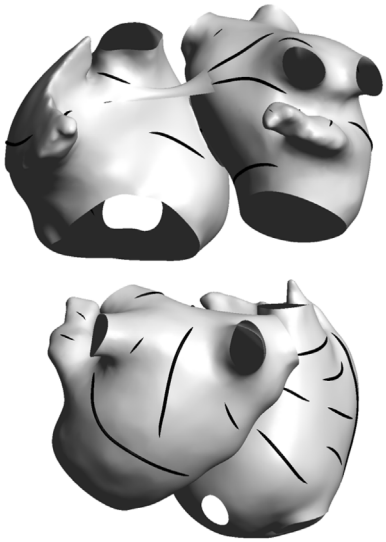

Fig. 9. Example of fiber orientation specification in the epicardium (anterior and posterior views). The fiber tracts manually drawn for constructing the orientation field by interpolation (Fig. 8, left panels) are shown as black lines.

is increased (panel A). Although the 'distance' method performs better for very few seed points, the methods become similar for large n_{seeds}. Little improvement is observed beyond n_{seeds} = 1000. As shown in panel B, there is a linear relation between d_{avg} and d_{sep}, which gives a way to specify d_{sep} based on the desired value of d_{avg}.

Streamline length is further analyzed in Fig. 7 that shows a typical distribution of lengths. Short streamlines (<1 cm) are most common as they are needed to fill the holes and achieve full coverage. On the other side of the spectrum, very long streamlines (>20 cm) are also generated that possibly wind several times around the geometry. The error bars on that figure provide a measure of variability between realizations of the

Table 1
Description of fiber orientation in the epicardium of the model displayed on Fig. 8. These statements may not be generally true in all patients.

	Comment and references
1	The Bachmann's bundle is represented as a separate surface for visualization. [35, Fig. 1], [36, Fig. 2a]
2	Fiber orientation in the left atrial roof follows the septopulmonary bundle. [35, Fig. 2b], [5, Fig. 5E]
3	Circumferential fibers run around the mitral and tricuspid valves. [14, Fig. 2], [9, Figs. 1 and 7], [10, Fig. 2], [8, Fig. 2], [16, Fig. 3]
4	Fibers in the superior vena cava sleeve run longitudinally in the epicardium. [9, Fig. 7]
5	In the anterior part of the right atrium, fibers are interpolated between the Bachmann's bundle and the circumferential fibers around the tricuspid valve. [13, Fig. 1C] [14, Fig. 2], [36, Fig. 2a]
6	The right appendage has a complex fiber structure. Here the fibers run towards the extremities of the appendage. [5, Fig. 1F]
7	The sleeves of the pulmonary veins are composed of circular bundles. [36, Fig. 2d], [10, Fig. 2], [37, Fig. 2.3b], [38, Fig. 7C]
8	Between the pulmonary veins, fibers run towards the posterior wall. [36, Fig. 2c], [9, Figs. 1 and 7], [10, Fig. 2], [36, Fig. 6b], [39, Fig. 4B], [38, Fig. 6A,7C]
9	Near the right inferior pulmonary vein, fibers rotate towards the right atrium. [5, Fig. 5C]
10	There is an abrupt change of fiber orientation in the posterior wall of the left atrium. [36, Fig. 2c], [9, Figs. 1 and 7], [36, Fig. 6b], [38, Fig. 6A]
11	In the region of the crista terminalis, fibers are longitudinally oriented in the direction from superior to inferior vena cava. [9, Figs. 1 and 7], [10, Fig. 2]
12	Fibers coming from the intercaval bundle of the posterior right atrium wall run perpendicularly to the crista terminalis. [7, Fig. 2.4], [17, Fig. 4], [9, Figs. 1 and 7D]
13	In the epicardium of the right atrium free wall, fibers run parallel to the crista terminalis towards the right appendage. [9, Fig. 7D], [16, Fig. 3]
14	Fibers in the inferior vena cava run circularly. [9, Fig. 7D]

Table 2
Description of fiber orientation in the endocardium of the model displayed on Fig. 8. These statements may not be generally true in all patients.

	Comment and references
15	In the left appendage, fiber orientation differs in the epicardium and the endocardium and combines both longitudinal and circular fibers. [14, Fig. 2], [10, Fig. 2], [9, Fig. 8], [13, Fig. 1C], [38, Fig. 7C]
16	The endocardial sleeves of the superior vena cava are composed of circularly orientated bundles. [5, Fig. 5B]
17	In pulmonary veins, fibers can be oblique and longitudinal. [15, Fig. 2], [9, Fig. 1E], [40, Fig. S2], [41, Fig. 2]
18	Endocardial fibers run from the pulmonary vein region to the mitral valve. [5, Fig. 5B], [39, Fig. 4B]
19	Pectinate muscles run perpendicularly to the crista terminalis. [9, Fig. 7C], [10, Fig. 2], [5, Fig. 7]. These endocardial fibers are only intended to represent the smaller bundles of the pectinates muscles. Thicker bundles require separate geometrical structures [13,26].

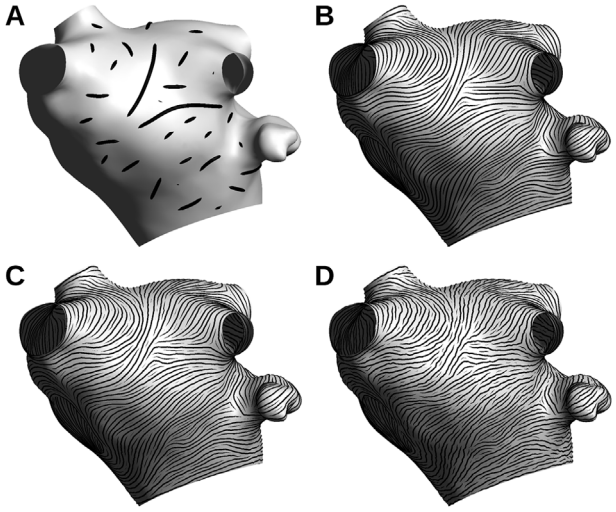

Fig. 10. More complex example of fiber orientation specification in the anterior left atrium. (A) Manually drawn fiber tracts; (B) interpolated orientation field; (C) random normal noise (standard deviation of 5°) added to the fiber angles of panel B; (D) noise standard deviation increased to 10°.

(random) streamline generation process.

3.4. Examples of fiber orientation field

Fig. 8 gives an example of visualization of fiber orientation in an atrial model (left and right atria; epicardial and endocardial surfaces). The fiber tracts used for orientation field interpolation are displayed in Fig. 9. Our aim was to display on our atrial geometry a fiber structure based on published models. We only attempted to reproduce the major features that were present in these models (as far as our eyes could guess from published figures) and suited to a surface representation. The choices involved in fiber orientation specification in the vicinity of the circled numbers on Fig. 8 are described in Tables 1 and 2.

Realistic atrial fiber orientation is more complex and less smooth than typical rule-based orientation. Experimentally-derived datasets may include spurious fibers, noise and artifacts. To give some insights into the impact of these difficulties, a less coherent set of fiber tracts was designed (Fig. 10A). The resulting streamlines feature abrupt changes in orientation but remain smooth (panel B). When uncorrelated random normal noise (standard deviation of 5°) is added to the local orientation angles, streamlines tend to be shorter and less smooth (panel C). With a noise standard deviation increased to 10° (panel D), some streamlines seem to propagate like cracks.

4. Discussion

We have extended and implemented an evenly-spaced streamline placement algorithm for visualization of orientation fields on a triangulated surface. The approach was found to be appropriate for displaying fiber orientation on an atrial geometry. Its clarity was somewhat reminiscent of manual drawings by anatomists. The visualization can be enriched by superimposing a color-coded scalar field on the surface. Longitudinal or transverse conductivity, the anisotropy ratio, or an activation map may be displayed on top of fiber orientation. Colorful fluid dynamics examples can be found in Ref. [18].

Two main parameters controlling the graphical representation were involved: the minimal inter-streamline distance d_{sep} and the number of seed points n_{seeds} per iteration. The number of streamlines drawn is of the order of the spatial extent of the surface divided by d_{sep}. The number of seed points enables a trade-off between visual quality and speed. In addition, the angle threshold for U-turn detection (stopping criterion 4) could be adjusted if needed but the value $\pi/2$ was found to be adequate in all cases tested. Finally, for the 'distance' placement method, the parameter c_{seed} was set to 1.3 following the recommendation for 2D grids [20]. The outcome was not found to be sensitive to the choice of c_{seed}. As in the 2D case [20], the choice of placement method relies on subjective assessment of aesthetics. As a rule of thumb, if n_{seeds} is very small, the 'distance' method provides a good guess for seed points, and,

in contrast, when n_{seeds} is very large, the 'random' approach explores a broader region of seed point locations.

The implementation was intended for use with d_{sep} of the order of Δx. When $d_{sep} \ll \Delta x$, the edge bit-mask may have to be extended and the assumption of constant vector field within each triangle may not be valid at that resolution. When $d_{sep} \gg \Delta x$, the approximation of geodesic distance by Euclidean distance may eventually become poor. The pre-calculation of edge neighborhood over a radius of d_{sep} also becomes more computationally expensive. Computational speed was however not our main focus since fiber orientation is not dynamic in simulations (unlike flow velocity fields). Streamlines were calculated and visualized in separate programs.

Among the limitations of the streamline approach, the orientation field is assumed to be relatively smooth, with the possible exception of some discontinuities (singularities). If the concept of local fiber orientation does not accurately represent the nature of tissue microstructure or when no fiber tract can be identified, our method may not outperform vector field quiver plots. Isotropic regions and fiber crossing cannot be described by a single vector field (two layers might be a solution in that case). Also, the surface must be a manifold. Inter-atrial connections and the inter-atrial septum need to be displayed as separate surfaces. Finally, the vector field is assumed to be tangent to the surface. The normal component is simply ignored, but could be color-coded if present.

Fig. 3 suggests applications of streamline placement beyond visualization, including anisotropic surface remeshing, subdivision and parameterization, and distribution of points over a surface.

5. Conclusion

Translation of fluid dynamics visualization techniques to orientation fields on a surface enabled us to produce clear representations of fiber orientation on the atrial surface. The distance between streamlines can be controlled and parameters can be adjusted to provide a trade-off between quality and speed. This evenly-spaced streamline visualization approach would facilitate the description and the comparison of fiber structure in computer models of the atria.

Conflict of interest statement

None declared.

Acknowledgments

This work was supported by the Natural Sciences and Engineering Research Council of Canada (NSERC grant RGPIN-2015-05658).

References

[1] N.A. Trayanova, Mathematical approaches to understanding and imaging atrial fibrillation: significance for mechanisms and management, Circ. Res. 114 (9) (2014) 1516–1531, https://doi.org/10.1161/CIRCRESAHA.114.302240.

[2] J. Zhao, T.D. Butters, H. Zhang, A.J. Pullan, I.J. LeGrice, G.B. Sands, B.H. Smaill, An image-based model of atrial muscular architecture: effects of structural anisotropy on electrical activation, Circulation. Arrhythmia and Electrophysiology 5 (2) (2012) 361–370, https://doi.org/10.1161/CIRCEP.111.967950.

[3] S.Y. Ho, R.H. Anderson, D. Sánchez-Quintana, Atrial structure and fibres: morphologic bases of atrial conduction, Cardiovasc. Res. 54 (2) (2002) 325–336.

[4] M. Varela, J. Zhao, O.V. Aslanidi, Determination of atrial myofibre orientation using structure tensor analysis for biophysical modelling, International Conference on Functional Imaging and Modeling of the Heart, Springer, 2013, pp. 425–432.

[5] F. Pashakhanloo, D.A. Herzka, H. Ashikaga, S. Mori, N. Gai, D.A. Bluemke, N.A. Trayanova, E.R. McVeigh, Myofiber architecture of the human atria as revealed by submillimeter diffusion tensor imaging, Circulation. Arrhythmia and Electrophysiology 9 (4) (2016) e004133, , https://doi.org/10.1161/CIRCEP.116.004133.

[6] S.Y. Ho, D. Sánchez-Quintana, The importance of atrial structure and fibers, Clin. Anat. 22 (1) (2009) 52–63, https://doi.org/10.1002/ca.20634.

[7] M.W. Krüger, Personalized Multi-Scale Modeling of the Atria: Heterogeneities, Fiber Architecture, Hemodialysis and Ablation Therapy, Ph.D. thesis Karlsruhe Institute of Technology, 2013, https://doi.org/10.5445/KSP/1000031226.

[8] T.E. Fastl, C. Tobon-Gomez, A. Crozier, J. Whitaker, R. Rajani, K.P. McCarthy, D. Sanchez-Quintana, S.Y. Ho, M.D. O'Neill, G. Plank, M.J. Bishop, S.A. Niederer, Personalized computational modeling of left atrial geometry and transmural myofiber architecture, Med. Image Anal. 47 (2018) 180–190, https://doi.org/10.1016/j.media.2018.04.001.

[9] C. H. Roney, A. Pashaei, M. Meo, R. Dubois, P. M. Boyle, N. A. Trayanova, H. Cochet, S. A. Niederer, E. J. Vigmond, Universal Atrial Coordinates Applied to Visualisation, Registration and Construction of Patient Specific Meshes, arXiv:1810.06630 [physics, q-bio]arXiv:1810.06630.

[10] J. M. Hoermann, M. R. Pfaller, L. Avena, C. Bertoglio, W. A. Wall, Automatic Mapping of Atrial Fiber Orientations for Patient-specific Modeling of Cardiac Electromechanics Using Image-Registration, arXiv:1812.02587 [physics] arXiv:1812.02587.

[11] K.S. McDowell, F. Vadakkumpadan, R. Blake, J. Blauer, G. Plank, R.S. MacLeod, N.A. Trayanova, Methodology for patient-specific modeling of atrial fibrosis as a substrate for atrial fibrillation, J. Electrocardiol. 45 (6) (2012) 640–645.

[12] V. Jacquemet, N. Virag, Z. Ihara, L. Dang, O. Blanc, S. Zozor, J.-M. Vesin, L. Kappenberger, C. Henriquez, Study of unipolar electrogram morphology in a computer model of atrial fibrillation, J. Cardiovasc. Electrophysiol. 14 (10 Suppl) (2003) S172–S179.

[13] M. Potse, A. Gharaviri, S. Pezzuto, A. Auricchio, R. Krause, S. Verheule, U. Schotten, Anatomically-induced fibrillation in a 3D model of the human atria, Computing in Cardiology, 2018.

[14] C. Tobón, C.A. Ruiz-Villa, E. Heidenreich, L. Romero, F. Hornero, J. Saiz, A three-dimensional human atrial model with fiber orientation. Electrograms and arrhythmic activation patterns relationship, PLoS One 8 (2) (2013) e50883, , https://doi.org/10.1371/journal.pone.0050883.

[15] O.V. Aslanidi, M.A. Colman, M. Varela, J. Zhao, B.H. Smaill, J.C. Hancox, M.R. Boyett, H. Zhang, Heterogeneous and anisotropic integrative model of pulmonary veins: computational study of arrhythmogenic substrate for atrial fibrillation, Interface Focus 3 (2) (2013) 20120069, https://doi.org/10.1098/rsfs.2012.0069.

[16] M. Varela, M.A. Colman, J.C. Hancox, O.V. Aslanidi, Atrial heterogeneity generates Re-entrant substrate during atrial fibrillation and anti-arrhythmic drug action: mechanistic insights from canine atrial models, PLoS Comput. Biol. 12 (12) (2016) e1005245, , https://doi.org/10.1371/journal.pcbi.1005245.

[17] A. Goette, J.M. Kalman, L. Aguinaga, J. Akar, J.A. Cabrera, S.A. Chen, S.S. Chugh, D. Corradi, A. D'avila, D. Dobrev, EHRA/HRS/APHRS/SOLAECE expert consensus on atrial cardiomyopathies: definition, characterization, and clinical implication, Ep Europace 18 (10) (2016) 1455–1490.

[18] T. McLoughlin, R.S. Laramee, R. Peikert, F.H. Post, M. Chen, Over two decades of integration-based, geometric flow visualization, Computer Graphics Forum, vol. 29, Wiley Online Library, 2010, pp. 1807–1829.

[19] G. Turk, D. Banks, Image-guided streamline placement, Proceedings of the 23rd Annual Conference on Computer Graphics and Interactive Techniques, ACM, 1996, pp. 453–460.

[20] B. Jobard, W. Lefer, Creating evenly-spaced streamlines of arbitrary density, Visualization in Scientific Computing'97, Springer, 1997, pp. 43–55.

[21] Z. Liu, R. Moorhead, J. Groner, An advanced evenly-spaced streamline placement algorithm, IEEE Trans. Vis. Comput. Graph. 12 (5) (2006) 965–972.

[22] K. Wu, Z. Liu, S. Zhang, R.J. Moorhead II, Topology-aware evenly spaced streamline placement, IEEE Trans. Vis. Comput. Graph. 16 (5) (2010) 791–801.

[23] O. Mattausch, T. Theussl, H. Hauser, E. Gröller, Strategies for interactive exploration of 3D flow using evenly-spaced illuminated streamlines, Proceedings of the 19th Spring Conference on Computer Graphics, ACM, 2003, pp. 213–222.

[24] B. Spencer, R.S. Laramee, G. Chen, E. Zhang, Evenly spaced streamlines for surfaces: an image-based approach, Computer Graphics Forum, vol. 28, Wiley Online Library, 2009, pp. 1618–1631.

[25] X. Mao, Y. Hatanaka, H. Higashida, A. Imamiya, Image-guided streamline placement on curvilinear grid surfaces, Visualization'98. Proceedings, IEEE, 1998, pp. 135–142.

[26] D. Harrild, C. Henriquez, A computer model of normal conduction in the human atria, Circ. Res. 87 (7) (2000) E25–E36.

[27] M.S. Floater, Mean value coordinates, Comput. Aided Geomet. Des. 20 (1) (2003) 19–27.

[28] The CGAL Project, 13 Edition, CGAL User and Reference Manual vol. 4, CGAL Editorial Board, 2018 URL https://doc.cgal.org/4.13/Manual/packages.html.

[29] G. Alessandrini, R. Magnanini, The index of isolated critical points and solutions of elliptic equations in the plane, Ann. della Scuola Norm. Super. Pisa - Cl. Sci. 19 (4) (1992) 567–589.

[30] D. Shreiner, G. Sellers, J. Kessenich, B. Licea-Kane, OpenGL Programming Guide: the Official Guide to Learning OpenGL, Version 4.3, Addison-Wesley, 2013.

[31] C.H. Roney, C.D. Cantwell, J.D. Bayer, N.A. Qureshi, P.B. Lim, J.H. Tweedy, P. Kanagaratnam, N.S. Peters, E.J. Vigmond, F.S. Ng, Spatial resolution requirements for accurate identification of drivers of atrial fibrillation, Circ. Arrhythmia. Electrophysiol. 10 (5) (2017) e004899, , https://doi.org/10.1161/CIRCEP.116.004899.

[32] V. Jacquemet, Phase singularity detection through phase map interpolation: theory, advantages and limitations, Comput. Biol. Med. 102 (2018) 381–389, https://doi.org/10.1016/j.compbiomed.2018.07.014.

[33] M. Dupraz, V. Jacquemet, Geometrical measurement of cardiac wavelength in reaction-diffusion models, Chaos (Woodbury, N.Y.) 24 (3) (2014) 033133, , https://doi.org/10.1063/1.4895811.

[34] V. Jacquemet, Modeling left and right atrial contributions to the ECG: a dipole-current source approach, Comput. Biol. Med. 65 (2015) 192–199, https://doi.org/10.1016/j.compbiomed.2015.06.007.

[35] M.J.H. van Campenhout, A. Yaksh, C. Kik, P.P. de Jaegere, S.Y. Ho, M.A. Allessie, N.M.S. de Groot, Bachmann's bundle: a key player in the development of atrial fibrillation? Circ. Arrhythmia. Electrophysiol. 6 (5) (2013) 1041–1046, https://doi.org/10.1161/CIRCEP.113.000758.

[36] D. Sánchez-Quintana, J.R. López-Mínguez, Y. Macías, J.A. Cabrera, F. Saremi, Left atrial anatomy relevant to catheter ablation, Cardiol. Res. Pract. (2014), https://doi.org/10.1155/2014/289720.

[37] A. Ferrer, R. Sebastián, D. Sánchez-Quintana, J.F. Rodríguez, E.J. Godoy, L. Martínez, J. Saiz, Detailed anatomical and electrophysiological models of human atria and Torso for the simulation of atrial activation, PLoS One 10 (11) (2015) e0141573, , https://doi.org/10.1371/journal.pone.0141573.

[38] J. Zhao, B. J. Hansen, Y. Wang, T. A. Csepe, L. V. Sul, A. Tang, Y. Yuan, N. Li, A. Bratasz, K. A. Powell, A. Kilic, P. J. Mohler, P. M. L. Janssen, R. Weiss, O. P. Simonetti, J. D. Hummel, V. V. Fedorov, Three-dimensional integrated functional, structural, and computational mapping to define the structural "Fingerprints" of heart-specific atrial fibrillation drivers in human heart ex vivo, J. Am. Heart Assoc. 6 (8). doi:10.1161/JAHA.117.005922.

[39] Jichao Zhao, J. Hansen Brian, A. Csepe Thomas, Praise Lim, Yufeng Wang, Michelle Williams, J. Mohler Peter, M.L. Janssen Paul, Raul Weiss, D. Hummel John, V. Fedorov Vadim, Integration of high-resolution optical mapping and 3-dimensional micro-computed tomographic imaging to resolve the structural basis of atrial conduction in the human heart, Circ. Arrhythmia. Electrophysiol. 8 (6) (2015) 1514–1517, https://doi.org/10.1161/CIRCEP.115.003064.

[40] C.H. Roney, J.D. Bayer, H. Cochet, M. Meo, R. Dubois, P. Jaïs, E.J. Vigmond, Variability in pulmonary vein electrophysiology and fibrosis determines arrhythmia susceptibility and dynamics, PLoS Comput. Biol. 14 (5) (2018) e1006166, , https://doi.org/10.1371/journal.pcbi.1006166.

[41] M. Hocini, S.Y. Ho, T. Kawara, A.C. Linnenbank, M. Potse, D. Shah, P. Jaïs, M.J. Janse, M. Haïssaguerre, J.M.T. De Bakker, Electrical conduction in canine pulmonary veins: electrophysiological and anatomic correlation, Circulation 105 (20) (2002) 2442–2448.